Applied Materials Today 20 (2020) 100694

Contents lists available at ScienceDirect

Applied Materials Today

journal homepage: www.elsevier.com/locate/apmt

Magnesium-based micromotors for enhanced active and synergistic hydrogen chemotherapy

Kun Liu[a,*], Juanfeng Ou[a], Shuanghu Wang[a], Junbin Gao[a], Lu Liu[a], Yicheng Ye[a], Daniela A. Wilson[b], Yunrui Hu[a,*], Fei Peng[c,*], Yingfeng Tu[a,*]

[a] Guangdong Provincial Key Laboratory of New Drug Screening, School of Pharmaceutical Science, Southern Medical University, Guangzhou 510515, China
[b] Institute for Molecules and Materials, Radboud University, Nijmegen, 6525 AJ, Netherlands
[c] School of Materials Science and Engineering, Sun Yat-Sen University, Guangzhou 510275, China

ARTICLE INFO

Article history:
Received 21 February 2020
Revised 5 April 2020
Accepted 5 May 2020

Keywords:
Magnesium
Micromotor
Reactive oxygen species
Active hydrogen
Chemotherapy

ABSTRACT

Hydrogen therapy has recently emerged as an attractive approach for combating major diseases including cancer, diabetes, stroke and Parkinson's disease. Herein, we ingeniously fabricated a fully biodegradable Magnesium (Mg) based micromotor for the active hydrogen and chemotherapeutics delivery, and firstly proposed the concept of a self-propelled micromotor platform used for cancer active hydrogen-chemotherapy. By consuming water, the micromotor generates sufficient hydrogen in-situ, which is not only propellant for motion, but also active component for hydrogen therapy. The active motion of micromotors with a speed up to 57 ± 19 $\mu m \bullet s^{-1}$ leads to enhanced diffusion of produced hydrogen that allows for higher extracellular and intracellular reducibility. Compared with the non-motor control, the micromotor loaded with doxorubicin improves the chemotherapy efficacy significantly by 2.4 times for 4T1 tumor cells with a concentration as low as 100 $\mu g \bullet mL^{-1}$. These results indicate that the Mg-based micromotors can act as self-propelled carriers for enhanced intracellular hydrogen and cancer chemotherapy. Taking advantage of the locally hydrogen generation and the active moving capabilities, the facilely engineered Mg micromotor provides great promise for cancer synergistic hydrogen chemotherapy.

1. Introduction

Nowadays, chemotherapy is still one of the major solutions for cancer treatment. However, the unsatisfied delivery efficiency and serious adverse effects of chemotherapeutic agents hinder the cure of cancer [1–3]. Hence, improving the sensitivity of cancer cells to anticancer drugs and drug delivery efficiency become a key issue to be considered for cancer therapy [4,5]. Hydrogen (H_2), as a kind of endogenous gas with physiological/pathological regulation functions and high bio-safety, has been confirmed as a powerful therapeutic antioxidant that can scavenge cytotoxic oxygen radicals of major diseases such as cancer, diabetes, stroke, Alzheimers and Parkinson's disease [6–12]. According to the literature, elevated levels of reactive oxygen species (ROS) are commonly found in cancerous tissues [13]. The increased ROS not only are oncogenic, but also act as signaling molecules for abnormal cell growth, metastasis, resistance to apoptosis, angiogenesis and differentiation block in lung, breast or colon cancer [14,15]. Recent studies have proved that either increase or decrease of rightly overexpressed ROS level in cancer cells could break the redox homoeostasis, thus resulting in the apoptosis of cancer cells [16,17]. Hence, scavenging ROS could be used as a new strategy for the cancer therapy.

It is interesting that H_2 has been confirmed to inhibit the proliferation of tumor cells by scavenging ROS and further disturbing the cellular redox homeostasis, without affecting the normal cells [6,12,18]. It is commonly accepted that the anti-oxidative H_2 could selectively reduce the highly-oxidative toxic radicals such as hydroxylradical [7,9,10,19–21]. Besides, it has been recently reported that H_2 could also down-regulate of pro-inflammatory cytokines and activate endogenous antioxidant enzymes such as superoxide dismutase (SOD) and catalase to perform the antioxidant effect [6]. However, the nonpolarity and low solubility of H_2 under the physiological conditions result in limited therapeutic efficacy. To overcome the undesired performance of H_2, various H_2 carriers including $PdH_{0.2}$ nanocrystals, MgB_2 Nanosheet and Fe nanoparticles were fabricated to achieve the storage, targeted delivery and controlled release of H_2 [18–20,22,23]. However, those approaches rely on H_2 loaded porous nondegradable micro and nanoparticles, which are of limited loading capacity, tissue penetration capability and biocompatibility. In addition, all the H_2 delivery until now

* Corresponding authors.
E-mail addresses: liukun_gdou@163.com (K. Liu), yunruihu@smu.edu.cn (Y. Hu), pengf26@mail.sysu.edu.cn (F. Peng), tuyingfeng1@smu.edu.cn (Y. Tu).

https://doi.org/10.1016/j.apmt.2020.100694
2352-9407/

were based on the passive diffusion, which may restrict the dissolution of H_2 in aqueous solution. Therefore, how to improve the H_2 delivery efficacy is still challenging.

Micro-/nanomotors that can convert chemical or physical energies into mechanical motion have attracted considerable attentions for their promising biomedical applications for example diagnosis [24,25], minimally invasive surgery [26–28], active drug delivery [29–35]. Especially for active drug delivery, the active motion of micro-/nanomotors endowed them huge advantages compared to their passive counterparts [36–40], which could be suitable perfectly for improving tumor therapeutic effect [30,41–47]. To take advantage of tumor inhibition from H_2, the active delivery of H_2 and chemotherapeutics may function as a novel strategy to further improve the synergistic therapeutic effects towards cancer.

Among different types of micromotors, the Mg-based Janus micromotors show great potential towards in vivo applications owing to their autonomous propulsion under body fluids, cargo transport and release, and their transient biodegradability [48-51]. Compared with other transition (Zn, Fe), or alkali metals (Na, Ca), Mg is of particular interest with a tailored degradation behavior under physiological or buffer conditions. Hence the speed and motion time of Mg based micromotors can be easily tuned either by ions or the design of micromotor [52]. Moreover, the controllable motion of Mg-based micromotor under blood plasma without any addition of external toxic fuels endows it a fascinating prospect for biomedical application [24,53,54]. In our case, most importantly, the capability of self-sacrificing and water-consuming (into H_2) allows Mg micromotors to be a clean and ideal H_2 generator and the formed H_2 is also the propellant for motion.

Here, we demonstrate the design of organic-inorganic hybrid Mg micromotor for enhanced active and synergistic hydrogen chemotherapy (Scheme 1). Biodegradable micromotors were fabricated by using Mg microparticles as templates and subsequently coating with poly(lactic-co-glycolic acid) (PLGA) asymmetrically, which is promising for drug delivery due to its degradable characteristics and improved drug loading capacity. The H_2 produced by Mg-water reaction was able to achieve enhanced diffusion due to the motion of micromotors, offering possibility for enhanced ROS scavenging (special for •OH) (Scheme 1C). By using Mg micromotors for active and synergistic hydrogen chemotherapy, an outstanding performance towards tumor cells was achieved (Scheme 1D).

2. Materials and methods

2.1. Materials

Mg microparticles (catalog FMW20; average size: 25 μm) were purchased from TangShan WeiHao Magnesium Powder Co. Poly(lactic-co-glycolic acid) (PLGA, 8000 Da) was bought from Jinan Daigang Biomaterial Co., Ltd. CellROX oxidative stress reagents (green) was purchased from Life Technologies Co. Methylene blue (MB), sodium dodecyl sulfate (SDS), doxorubicin (DOX), methylthiazolyldiphenyl-tetrazolium bromide (MTT), and dimethyl sulfoxide (DMSO) were obtained from Sigma-Aldrich. 2, 7-dichlorodihydrofluorescein diacetate (DCFH-DA), calcein O, O-diacetate tetrakis (acetoxymethyl) ester/propidium iodide (calcein-AM/PI) and 4,6-diamidino-2-phenylindole (DAPI) were purchased from Beyotime Biotechnology. Human colon cancer cell line (HT29) and rat breast cancer cell line (4T1), obtained from American Type Culture Collection (ATCC), were used as model cancer cells to evaluate the active and synergistic hydrogen chemotherapy of Mg based motors. All reagents for cell culture were bought from Gibco. All other chemical regents used in this experiment were analytically pure without further purification.

2.2. Instruments

Scanning electron microscope (SEM) images were recorded on a Phenom emission scanning electron microscope. Energy-dispersive X-ray spectroscopy (EDX) element analysis was carried out with an EDX analyzer (mounted on the Phenom FEI-SEM Pharos) with an accelerating voltage of 15 kV. Nikon Ti2-A inversion fluorescence microscope were used to capture cell morphology and motion of Mg-motor. A Multi-function plate reader (Tecan, Infinite M1000 Pro, Swiss) was used to detect the cell fluorescence intensity.

2.3. Fabrication of Mg-motor and Mg-plga microparticles

Fabrication of Mg-motor: Mg microparticles were used as the core to prepare Mg-based micromotors (named as Mg-motor). The Mg microparticles were initially washed with acetone to remove the impurities, then dried under N_2 flow. Subsequently, 1 mg of Mg microparticles were dispersed onto a glass slide precoated with a thin film of poly(vinylpyrrolidinone) (PVP). After that, the formed Mg microparticles layer were coated with PLGA or the mixture of PLGA and DOX in ethyl acetate. The resulting Mg-motors were scraped carefully from the glass slide. The DOX loaded Mg-motor was named as Mg-motor-DOX.

Fabrication of Mg-PLGA microparticles: The same prewashing method as mentioned in 2.1 was used to fabricate Mg-PLGA microparticles that couldn't release hydrogen. Firstly, 100 μL of PVP ethyl alcohol solution (2 mg•mL^{-1}) was casted on a glass slide to form a thin film, followed by adding 60 μL of PLGA ethyl acetate solution (1 w/w%). Subsequently, 1 mg of Mg microparticles were dispersed onto the thin layer of PLGA, then another 60 μL of PLGA solution was added, so as to fabricate well encapsulated Mg-PLGA microparticles. The DOX loaded Mg-PLGA microparticle was named as Mg-PLGA-DOX.

2.4. Characterization of Mg-motor

Scanning electron microscope (SEM) images were obtained by a Phenom LE instrument (Phenom, Eindhoven, Netherlands) with an acceleration voltage of 10 kV. Energy-dispersive X-ray spectroscopy (EDX) element mapping was acquired by an EDX detector mounted on the Phenom FEI-SEM Pharos with an accelerating voltage of 15 kV and analyzed by ProSuite software. Before measurement, all samples were attached onto the conductive adhesives, then coated with platinum using a Quorum Q150V Plus ion sputtering system (Quorum Technologies Co., Ltd, Laughton, United Kingdom). Bight-field and fluorescent images of the Mg-motors were captured by Nikon microscope coupled with × 20 microscope objectives and fluorescence filter for red light excitation. The fluorescence and bright-filed images of Mg motor (stained with Nile red) were captured on Nikon Ti2-A inversion fluorescence microscope (Nikon Eclipse Instrument Inc.).

2.5. Motion of Mg-motor

The RPMI 1640 culture medium for HT29 and 4T1 cells was used as main solution of the simulated body fluid (SBF). And the movements of Mg-motor were evaluated in SBF supplemented with 0.3 M $NaHCO_3$ and 0.1% SDS at 37 °C to character the motion trajectory. A Nikon Ti2-A inverted optical microscope equipped with a high-speed camera (Nikon, DS-Qi2) and NIS Elements AR 3.2 software was used to observe and record the motion of Mg-motor with 10 frames per second (time interval between each frames ΔT = 100 ms). Tracking image sequences were analyzed with Image J plugin manual tracking according to the previous report[55]. At least 25 micromotors were tracked to calculate the average speeds.

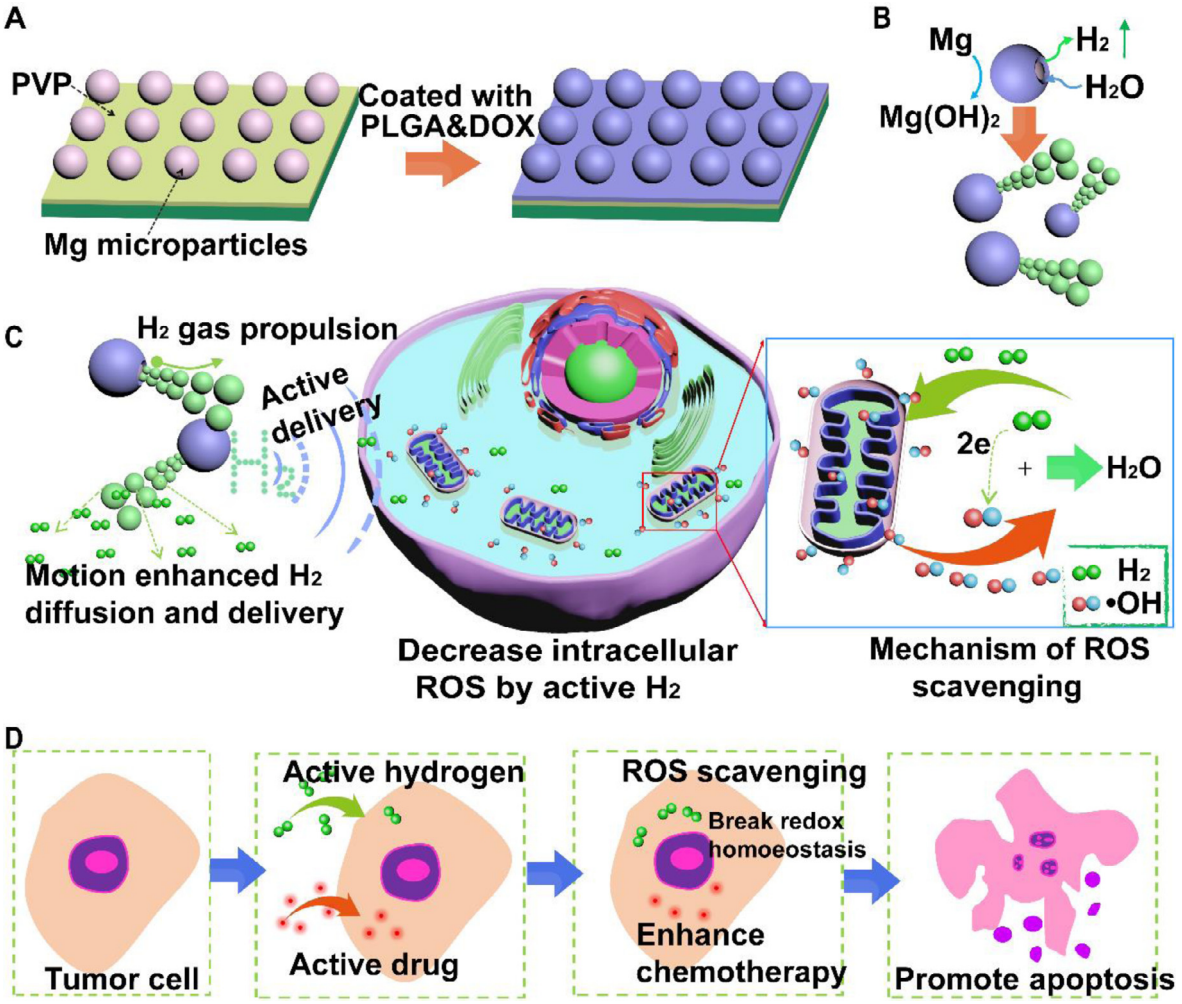

Scheme 1. (A) Schematic illustration of the fabrication of Mg-based micromotors; (B) Illustrations of the propulsion mechanism of Mg micromotors; (C) Schematic demonstration of Mg-based micromotors as Hydrogen generator and drug delivery platform for locally active H_2 generation to scavenge •OH; (D) Enhanced active hydrogen chemotherapy of Mg micromotors.

2.6. Measurement of the ROS level in cells

Measure intracellular ROS level by DCFH-DA probes: HT29 or 4T1 cells were seeded onto 96-well plate with density of 5×10^3 cells per well and cultivated in 100 μL RPMI 1640 culture medium. After 24 h, the culture medium was replaced by the fresh serum-free one containing the pure Mg microparticles with a series concentration of 0, 25, 50, 100, 150, 200 and 300 $\mu g \bullet mL^{-1}$ and $NaHCO_3$ (0.3 M). After incubated for 2 h, the medium was removed and each well was washed with the fresh serum-free RPMI 1640 culture medium to remove residual samples. Then, the DCFH-DA probes (100 μL, 10 μM) was added into each well and the resulting 96-well plate was monitored by a multi-mode microplate reader (excitation/emission = 488/525 nm). The fluorescence images of the two cells were obtained using an invert microscope after removing medium and washing three times with PBS.

Measure intracellular ROS level by CellROX probes: HT29 cells (2×10^5 mL^{-1}) or 4T1 cells (1×10^5 mL^{-1}) were seeded onto 12-well plate and cultivated in RPMI 1640 culture medium. After 48 h, the culture medium was replaced by fresh serum-free ones containing the prepared samples with final concentrations of 300 $\mu g \bullet mL^{-1}$ and $NaHCO_3$ (0.3 M). After incubated for 6 h, the medium was removed and each well was washed with the fresh serum-free RPMI 1640 culture medium to remove residual samples. Then, the CellROX probes (200 μL, 5 μM) was added, and incubated for 30 min at 37 °C. Then remove medium and wash the cells for 3 times with PBS, and fix the cells with 3.7% formaldehyde for 15 min. After washing 3 times with PBS, the cells were stained by an antifade Mounting Medium with DAPI. The ROS changing of the cells was analyzed by using an Olympus fluorescent microscope.

2.7. Measurement of DOX uptake efficacy of cancer cell

HT29 or 4T1 cells with density of 1×10^4 cells per well were seeded onto 24-well plates and cultivated in RPMI 1640 for 48 h. Subsequently, the culture medium was replaced by fresh serum-free ones containing Mg-motor-DOX and Mg-PLGA-DOX (150 $\mu g \bullet mL^{-1}$) and $NaHCO_3$ (0.3 $mol \bullet L^{-1}$) and co-cultured for 6 h. Then the cells were washed with PBS for 3 times before staining with DAPI (final concentration 10 $\mu g \bullet mL^{-1}$, 10 min). Finally, the cell were washed with PBS and the fluorescence images were captured on Nikon Ti2-A inversion fluorescence microscope.

2.8. Cytotoxicity analysis

HT29 or 4T1 cells with density of 5×10^3 cells per well were seeded onto 96-well plates and cultivated in RPMI 1640 medium for 24 h. Then the cells were incubated respectively with Mg-motor-DOX, Mg-motor, Mg-PLGA-DOX, Mg and Mg-PLGA in RPMI

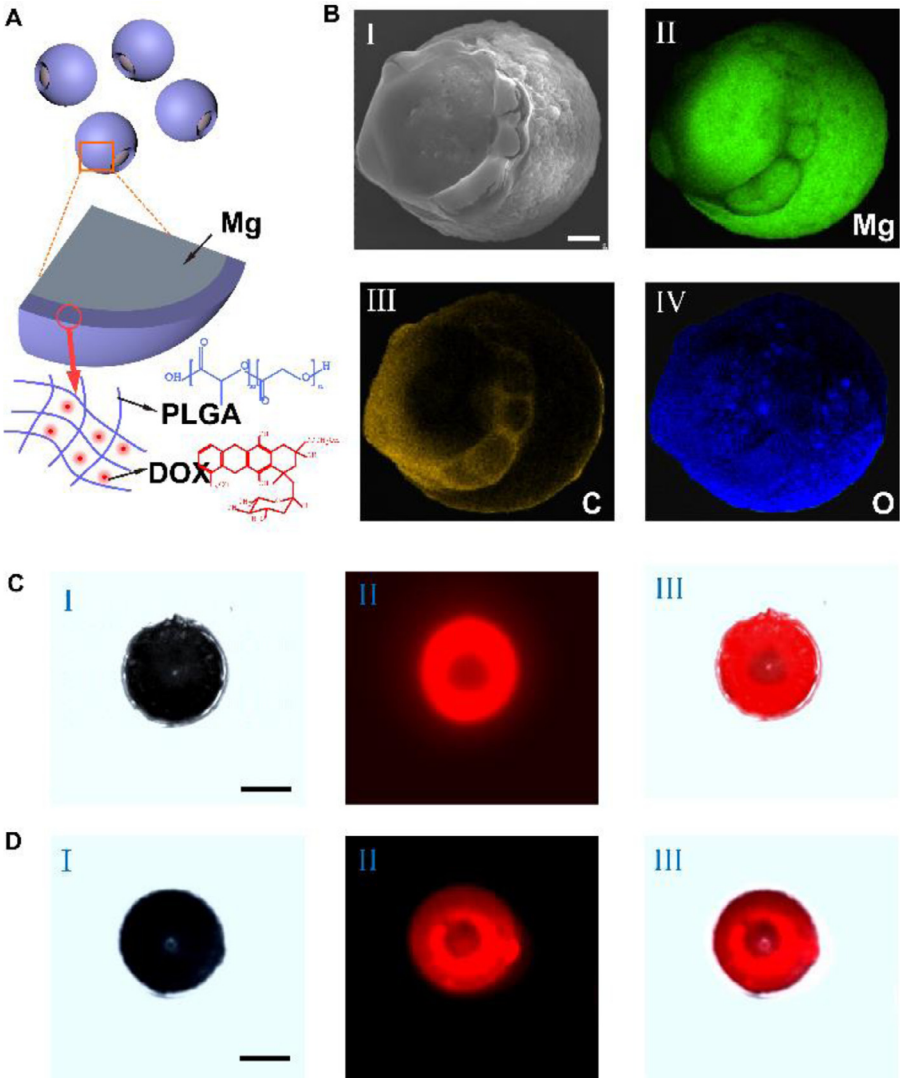

Fig. 1. (A) Schematic illustration of the structure of Mg based micromotors; (B) SEM and EDX characterizations of the Mg-based micromotor (I: SEM image; II-IV: EDX map images of Mg, C and O). Scale bar: 5 μm. (C) Brightfield (I) and fluorescence (II) microscopy visualization of Mg-motor fabricated with PLGA and Nile red labelled (Red). Scale bar: 20 μm. (D) Brightfield (I) and fluorescence (II) microscopy visualization of Mg micromotor loaded with DOX (named as Mg-motor-DOX). Scale bar: 20 μm. (For interpretation of the references to color in this figure legend, the reader is referred to the web version of this article.)

1640 medium. After another 24 h incubation, the medium was carefully removed and the cells were washed twice with PBS. Subsequently, 110 µL MTT in fresh culture medium (0.5 mg•mL^{-1}) was added. After incubation for 4 h, the culture medium was carefully removed, and 100 µL DMSO was added per well, followed by 10 min shaking on a horizontal shaker. Biotek 800 TS plate reader was used to measure the absorbance at 490 nm.

3. Results and discussion

3.1. Fabrication and characterization of Mg micromotors

Mg microparticles were first imbedded onto the PVP film and further encapsulated with biodegradable PLGA [56]. After being scraped from the plates, a loophole was formed on one side of the resulting Mg microsphere. According to the scanning electron microscopy (SEM) images, the pure Mg microparticles exhibited a spherical structure with an average size of 23 ± 5 μm (Fig. S1a-c, Supporting Information). While after PLGA coating, the formed Mg micromotors (named as Mg-motor) displayed a spherical geometry with a small circular opening (Fig. 1A and B). Compared with the pure Mg microparticles, the Mg-motor was demonstrated a larger size (27 ± 5 μm, Fig. S1i, Supporting Information) owing to the coated PLGA shell. Energy dispersive X-ray spectroscopy (EDX) results in Fig. 1B illustrated the presence and elemental distribution of Mg from the core and C and O from PLGA shell within the micromotor structure. The pure Mg microparticle exhibited a smooth surface with less carbon covered when compared with that of micromotor (Fig. S2, Supporting Information). The typical Janus structure of the Mg-motor could be attributed to the partial Mg microparticles embedded in the PVP films on glass slides during PLGA coating. Due to the polymeric structure, hydrophobic Nile red or antitumor drug DOX was loaded into PLGA shell respectively, which further confirmed the asymmetric distribution of polymer layer on the Mg microparticles (Fig. 1C and D). The loading efficiency of DOX, calculated according to the standard curve of DOX (Fig. S3a, Supporting Information), was 33.61 μg•mg^{-1} (Fig. S3b, Supporting Information). In our work, the small opening of the Mg-motor could act as Mg-water reaction interface for H_2 generation under the gastric and intestine fluid or even serum environment, therefore resulting in the autonomous motion.

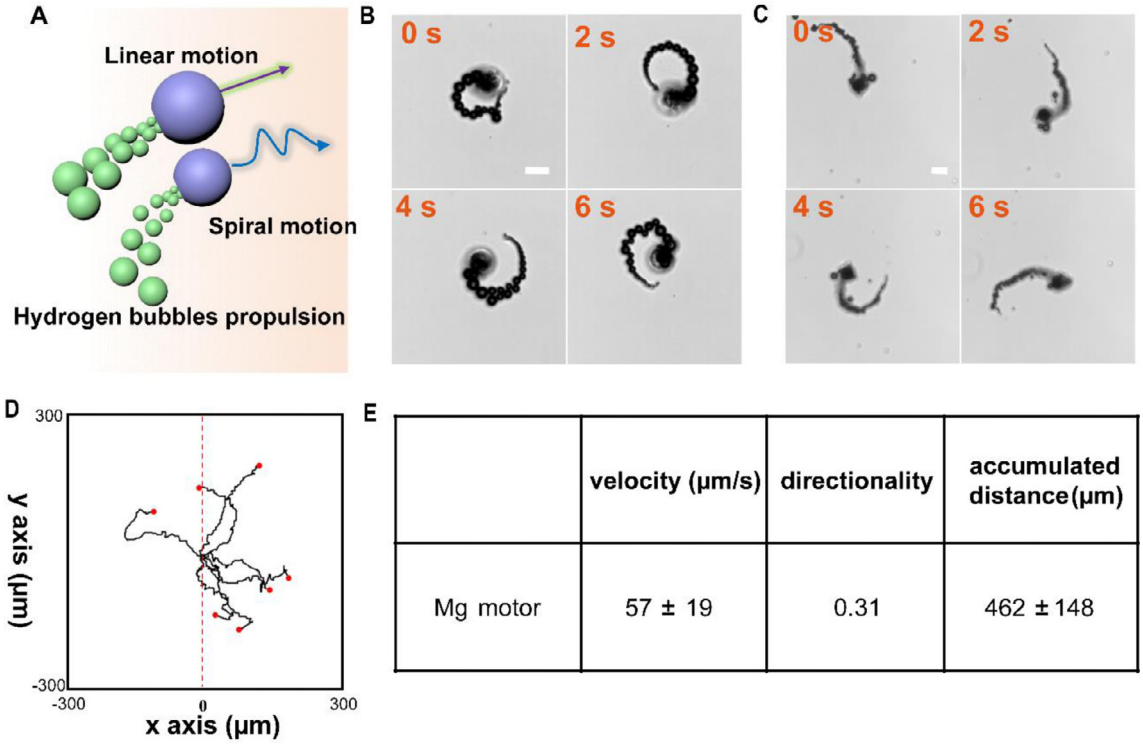

	velocity (μm/s)	directionality	accumulated distance (μm)
Mg motor	57 ± 19	0.31	462 ± 148

Fig. 2. Movement of Mg based micromotor in SBF. (A) Schematic illustration of Mg-based micromotor's movement by ejecting H_2. (B-C) Microscopy images (corresponding to Video S1 and Video S2, Supporting Information) displaying the spiral and linear-spiral motions of Mg based micromotor in SBF. (D) Tracking paths of Mg based micromotors at different directions. (E) Table of velocity, directionality, and accumulated distance of Mg based micromotors (25 micromotors analyzed).

3.2. Motion of Mg micromotors

After confirming the structure, we next evaluated the motion of the Mg-motor under SBF. According to the previous reports, the mobility of the micromotors could be affected by environmental factors such as components, viscosity and temperature[57]. When using nano/micromotors for purpose of biomedicine, the complicated component of biofluid could affect the motion behaviours of nano/micromotors [58–61]. Therefore, to precisely evaluate the motion enhanced H_2 and DOX delivery in cultured cancer cells, we chose the cell culture medium as the basic media to mimic the SBF environment. The schematic image in Fig. 2A illustrated that the continuous H_2 generation could propel Mg-motor to achieve autonomous motion in SBF. An invert microscopy was used to record the trajectory of the Mg-motor, which displayed different motion behaviors, such as spiral or linear mode (Fig. 2B-C; captured from Videos S1 and S2, Supporting Information). Image J with manual tracking module was further applied to analyze the trajectory path and the motion characteristics including average velocity, directionality, and accumulate distance (Fig. 2E). Owing to the gradual Mg depletion in SBF, the Mg-motor displayed a lifetime of ≈ 4.5 min with an average speed up to 57 ± 19 $\mu m \bullet s^{-1}$. It was noted that once the Mg core was fully depleted (i.e., completion of the Mg-proton reaction as shown in Video S3, Supporting Information), the Mg-motor stopped only with PLGA shell left (Fig. S4, Supporting Information), as illustrated in the corresponding Video S4 (Supporting Information).

3.3. Assessment of active hydrogen released by Mg micromotors

To evaluate the controlled release and bio-reductivity of H_2 in SBF, MB was used as an oxidative probe for H_2 detection. Generally, MB can react with H_2 in the presence of Pt (Pt nanoparticles 50 nm, Fig. S5, Supporting Information) to produce colorless reduced leucomethylene blue (leucoMB) according to the followed equation [62]:

$$MB\ (blue) + 2H^+ + 2e^- \rightarrow leucoMB\ (colorless) \quad (1)$$

Therefore, the color fading of MB was used to quantify the release of reductive H_2 from Mg microparticle, Mg-motor and Mg-PLGA respectively (Fig. S6, Supporting Information). As for the pure Mg microparticle, the absorbance of MB at 644 nm was sharply decreased in 20 min then increased afterwards, indicating the fast H_2 releasing (Fig. S7a, Supporting Information) owing to the rapid degradation of Mg in SBF. While for Mg-motor, it lasted for 40 min which was two times longer than that of Mg microparticle (Fig. S7b, Supporting Information). The prolonged and controlled H_2 release from Mg-motor was attributed to the gradual Mg depletion from the Janus structure. Besides, the well encapsulated Mg-PLGA microparticles exhibited a extremely lower H_2 release (Fig. S7c, Supporting Information). The intracellular reductivity of H_2 released from Mg-motor were also tested by the MB-Pt probe. As shown in Fig. S8 (Supporting Information), both 4T1 and HT29 stained with MB showed deep blue at 0 min. While the color was sharply decreased in 60 min then slightly increased afterwards (120 min) after incubating with Mg-motor. The decrease in color demonstrated that active H_2 release was possible to across cytomembrane and penetrate into cells, indicating the significant intracellular time-dependent bio-reductivity of Mg-motor.

Considering the bio-reducibility of H_2, the overexpressed ROS (especial for hydroxyl radical) in tumor cells could be eliminated by the active H_2 produced by Mg-motor. Fig. 3A shows schematically the experimental design of motion enhanced intracellular ROS scavenging. Fluorogenic ROS probe (CellROX Green reagent) was used to measure the ROS level in both two model cells. The cell-permeable CellROX is nonfluorescent in its reduced state while it binds onto DNA and becomes fluorescence upon oxidation. As shown in Fig. 3B-IV and 3E-IV, Mg-motor showed the highest ROS

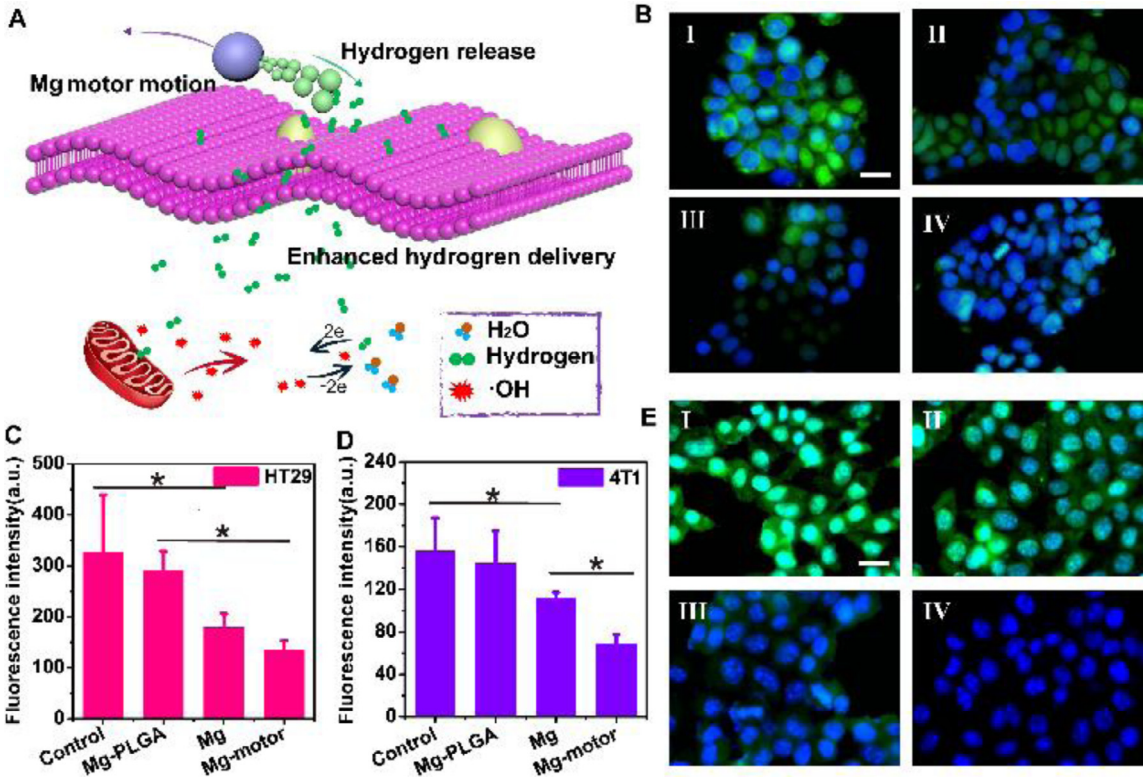

Fig. 3. Enhanced ROS scavenging ability of Mg-motor. (A) Schematic illustration of Mg-motor enhanced intracellular ROS scavenging; (B, E) Inverted fluorescence microscope images of ROS in HT29 (B) and 4T1 (E) cells measured by CellROX (I: control group; II–IV: experimental groups treated with Mg-PLGA, Mg and Mg-motor respectively), Scale bar: 20 μm; (C, D) Intracellular ROS levels in HT29 (C) and 4T1 (D) cells measured by DCFH-DA. (* $p<0.05$).

scavenging ability in both HT29 and 4T1 cells due to the motion enhanced H_2 diffusion and dissolution in aqueous as illustrated in Fig. S8 (Supporting Information). To further evaluate the ROS scavenging ability of Mg-motor, another ROS probe (DCFH-DA) was used to detect the intracellular ROS level. It should be noted that DCFH-DA can also permeate into cell, then be degraded by intracellular lipase and converted into DCFH. The formed DCFH can be further oxidized into fluorescent DCF, which has a positive correlation with intracellular ROS level. The fluorescence intensity of Mg-motor and Mg microparticles showed a significant decrease in both two cells (Fig. 3C-D, Fig. S9 in Supporting Information). It should be noted that Mg-motor exhibited over 12 times ROS scavenge efficacy than that of the passive microparticles (Fig. S10, Supporting Information). According to previous reports, H_2 could break redox homoeostasis, leading to the apotosis of cancer cells [6,20,22]. Hence, it is fascinating that the stronger ROS scanvenge ability of Mg-motor by delivering active H_2 could be a new stragey for cancer therapy.

3.4. Synergistic therapeutic effect of Mg motors in vitro

The motion of Mg-motor can be used not only to deliver active H_2 as we discussed above, but also to improve the drug delivery efficacy [52]. To verify synergistic therapeutic effect of Mg motors by coupling active delivery of H_2 and chemotherapeutic drug, DOX, which could inhibit the growth of tumor by interfering the function of DNA by inhibiting activity of topoisomerase II, has been chosen as the model drug loaded on the Mg-motor. After incubating with Mg-motor-DOX for 6 h, the intracellular uptake of DOX by two tumor cells was evaluated respectively. As shown in Fig. 4A-B, the intracellular DOX fluorescence was significantly increased in both 4T1 and HT29 cells, indicating that the motion of the micromotor could promote the uptake of DOX efficiently. While much less fluorescence was observed in HT29 cells, probably because of the difference between various tumor cells [63,64]. The semiquantitative analysis of intracellular DOX (Fig. 4C-D) was further calculated three times by Image J to obtain the average value of fluorescence intensity (see Supporting Information). It was interesting to find that the fluorescence intensity of DOX in 4T1 and HT29 cells was improved more than 17 and 5 times respectively when compared with non-motor groups (Mg-PLGA-DOX). Calcein-AM /PI kit was further used to test the ratio between living and death cells after treatment. The strongest red fluorescence (dead cells) was observed after incubating with Mg-motor-DOX due to combined hydrogenchemical therapy. (Fig. S11, Supporting Information) This suggested that the hydrogen chemotherapy had greater suppression on tumor cells, particularly for 4T1 cells, which could be ascribed to enhanced DOX therapeutic efficacy induced by synergistic effects of the active drug delivery and sustained hydrogen release.

We further evaluated the therapeutic effect of active hydrogenchemical therapy on both HT29 and 4T1 cells (Fig. 4E-F). No significant cytotoxicity was observed for Mg-PLGA (without H_2 production), Mg microparticles (passive H_2 delivery), Mg-motor (active H_2 delivery) and Mg-PLGA-DOX (single chemotherapy) when the Mg concentration was lower than 100 mg•mL^{-1}. However, lowest viability in both cancer cell lines especially for 4T1 cells was demonstrated when incubating with Mg-motor-DOX. (Fig. 4E-F) HT29 cells were less sensitive to DOX than 4T1 cells, which could be attributed to the drug resistance of cancer cells [63]. When the concentration of Mg-motor-DOX increased from 50 to 100 μg•mL^{-1} (DOX concentration was 1.5 to 3.0 μg•mL^{-1} accordingly), the viability of 4T1 cell decreased sharply from 92.37% to 31.00%, which exhibited remarkably improved cytotoxicity compared with DOX and other DOX loaded nanodrugs reported previously [65–74]. While for Mg-PLGA-DOX (non-motor), the viability decreased slightly from 91.34% (50 μg•mL^{-1}) to 75.43% (100

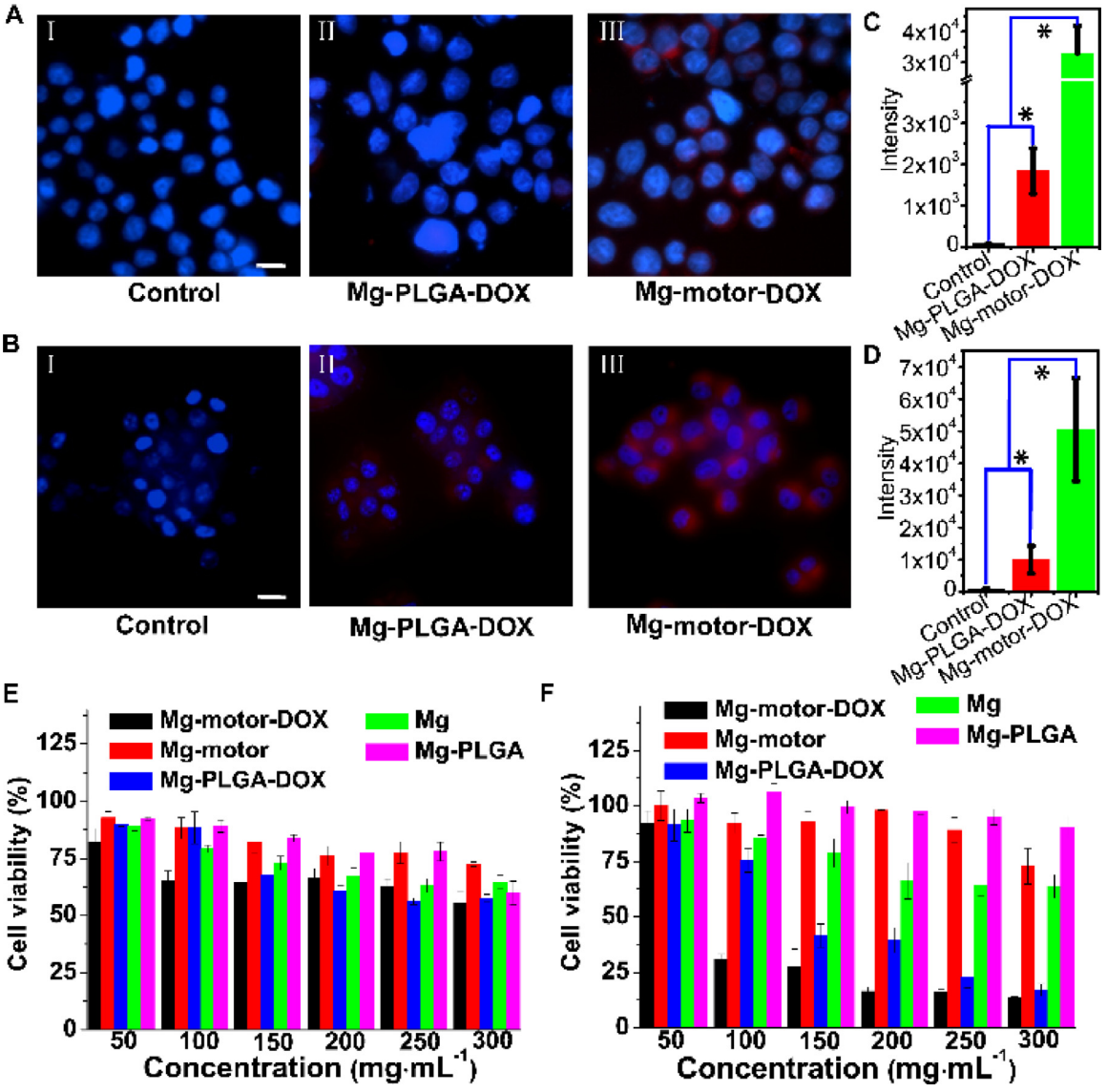

Fig. 4. DOX endocytosis and therapeutic efficacies of cancer cells. DOX uptake of HT29 (A) and 4T1 (B) (I: Control groups; II: Incubated with Mg-PLGA-DOX; III: Incubated with Mg-motor-DOX; scale bar is 20 μm); The calculated DOX fluorescence intensity of HT29 (C) and 4T1 (D) cells after incubated with Mg-motor-DOX and Mg-PLGA-DOX, the cells without adding any samples were used as control groups; Cell viability of HT29 (E) and 4T1 (F) after treatment of Mg-motor-DOX, Mg-motor, Mg-PLGA-DOX, Mg microparticles and Mg-PLGA. (* $p<0.05$).

μg•mL^{-1}). The huge difference in cell viability bewteen motor and non-motor groups demonstrated a significantly improved therapeutic effects due to the active H_2 induced enhanced sensitivity of cancer cells to DOX, indicating the superiority of combined active H_2 and enhanced chemotherapy. According to the results displayed above, it was obvious that such synergistic anticancer effects could be valuable to improve cancer therapeutic efficacy in future.

4. Conclusion

In summary, we demonstrated a facile approach for engineering a fully biodegradable Mg micromotor based H_2 generating system for active hydrogen chemotherapy for the first time. By consuming water in local biological environment, the designed Mg micromotors were able to propel in SBF efficiently. This leads to a controlled generation and enhanced diffusion of H_2 which allowed for higher intracellular ROS scavenging and redox homoeostasis re-establishment. The locally produced H_2 by Mg micromotors could further improve the sensitivity of tumor cells to chemotherapy. Due to the self-propulsion, Mg micromotors exhibited much higher drug delivery efficiency, resulting in enhanced chemotherapeutic efficacy. The concept of Mg micromotor based active hydrogenchemical therapy represent a concrete step towards clinical translation of hydrogen-chemo antitumor therapy. We envision that such artificial biodegradable micromotor delivery system could have wide applications in various diseases related with elevated ROS level by regulating the physiological/pathological functions.

Appendix A. supplementary data

Supplementary material related to this article can be found, in the online version.

Declaration of Competing Interests

The authors declare no conflicts of interest.

CRediT authorship contribution statement

Kun Liu: Conceptualization, Investigation, Writing - original draft. **Juanfeng Ou:** Investigation. **Shuanghu Wang:** Investigation. **Junbin Gao:** Investigation. **Lu Liu:** Investigation. **Yicheng Ye:** Validation. **Daniela A. Wilson:** Writing - review & editing. **Yunrui Hu:** Writing - review & editing. **Fei Peng:** Supervision. **Yingfeng Tu:** Conceptualization, Supervision, Writing - review & editing.

Acknowledgements

This work was supported by the National Natural Science Foundation of China (Grant No. 21805318, 51973241 and 31800835), Natural Science Foundation of Guangdong Province (2018B030306007 and 2018A030313521), Guangdong Basic and Applied Basic Research Foundation (2020A1515010173). The authors thank the support from the Chinese 1000-Talent Young Program and Pearl Youth Scholar Funded Scheme.

Supplementary materials

Supplementary material associated with this article can be found, in the online version, at doi:10.1016/j.apmt.2020.100694.

References

[1] X. Liang, C. Gao, L. Cui, S. Wang, J. Wang, Z. Dai, Self-assembly of an amphiphilic janus camptothecin-floxuridine conjugate into liposome-like nanocapsules for more efficacious combination chemotherapy in cancer, Adv. Mater. 29 (2017) 1703135 http://doi.org/10.1002/adma.201703135.

[2] I. Keklikoglou, C. Cianciaruso, E. Güç, M.L. Squadrito, L.M. Spring, S. Tazzyman, L. Lambein, A. Poissonnier, G.B. Ferraro, C. Baer, A. Cassará, A. Guichard, M.L. Iruela-Arispe, C.E. Lewis, L.M. Coussens, A. Bardia, R.K. Jain, J.W. Pollard, M. De Palma, Chemotherapy elicits pro-metastatic extracellular vesicles in breast cancer models, Nat. Cell Biol. 21 (2019) 190–202 http://doi.org/10.1038/s41556-018-0256-3.

[3] G.S. Karagiannis, J.M. Pastoriza, Y. Wang, A.S. Harney, D. Entenberg, J. Pignatelli, V.P. Sharma, E.A. Xue, E. Cheng, T.M.D. Alfonso, J.G. Jones, J. Anampa, T.E. Rohan, J.A. Sparano, J.S. Condeelis, M.H. Oktay, Neoadjuvant chemotherapy induces breast cancer metastasis through a TMEM-mediated mechanism, Sci. Transl. Med. 9 (2017) eaan0026 http://doi.org/10.1126/scitranslmed.aan0026 .

[4] Q. He, J. Shi, MSN Anti-cancer nanomedicines: chemotherapy enhancement, overcoming of drug resistance, and metastasis inhibition, Adv. Mater. 26 (2014) 391–411 http://doi.org/10.1002/adma.201303123.

[5] Q. Sun, Z. Zhou, N. Qiu, Y. Shen, Rational design of cancer nanomedicine: nanoproperty integration and synchronization, Adv. Mater. 29 (2017) 1606628 http://doi.org/10.1002/adma.201606628.

[6] Y. Wu, M. Yuan, J. Song, X. Chen, H. Yang, Hydrogen gas from inflammation treatment to cancer therapy, ACS Nano 13 (2019) 8505–8511 http://doi.org/10.1021/acsnano.9b05124.

[7] B. Zhang, F. Wang, H. Zhou, D. Gao, Z. Yuan, C. Wu, X. Zhang, Polymer dots compartmentalized in liposomes as a photocatalyst for in situ hydrogen therapy, Angew. Chem. Int. Ed. 58 (2019) 2744–2748 http://doi.org/10.1002/anie.201813066.

[8] L. Zhang, P. Zhao, C. Yue, Z. Jin, Q. Liu, X. Du, Q. He, Sustained release of bioactive hydrogen by Pd hydride nanoparticles overcomes Alzheimer's disease, Biomaterials 197 (2019) 393–404 http://doi.org/10.1016/j.biomaterials.2019.01.037.

[9] I. Ohsawa, M. Ishikawa, K. Takahashi, M. Watanabe, K. Nishimaki, K. Yamagata, K.-i. Katsura, Y. Katayama, S. Asoh, S. Ohta, Hydrogen acts as a therapeutic antioxidant by selectively reducing cytotoxic oxygen radicals, Nat. Med. 13 (2007) 688–694 http://doi.org/10.1038/nm1577.

[10] Y. He, B. Zhang, Y. Chen, Q. Jin, J. Wu, F. Yan, H. Zheng, Image-guided hydrogen gas delivery for protection from myocardial ischemia–reperfusion injury via microbubbles, ACS Appl. Mater. Interfaces 9 (2017) 21190–21199 http://doi.org/10.1021/acsami.7b05346.

[11] H. Chen, C. Zhou, K. Xie, X. Meng, Y. Wang, Y. Yu, Hydrogen-rich saline alleviated the hyperpathia and microglia activation via autophagy mediated inflammasome inactivation in neuropathic pain rats, Neuroscience 421 (2019) 17–30 http://doi.org/10.1016/j.neuroscience.2019.10.046.

[12] R. Asada, K. Kageyama, H. Tanaka, H. Matsui, M. Kimura, Y. Saitoh, N. Miwa, Antitumor effects of nano-bubble hydrogen-dissolved water are enhanced by coexistent platinum colloid and the combined hyperthermia with apoptosis-like cell death, Oncol. Rep. 24 (2010) 1463–1470 http://doi.org/10.3892/or_00001006.

[13] E. Panieri, M.M. Santoro, ROS homeostasis and metabolism: a dangerous liason in cancer cells, Cell Death Dis. 7 (2016) e2253 http://doi.org/10.1038/cddis.2016.105.

[14] P.L. de Sa Junior, D.A.D. Camara, A.S. Porcacchia, P.M.M. Fonseca, S.D. Jorge, R.P. Araldi, A.K. Ferreira, The roles of ROS in cancer heterogeneity and therapy, Oxid. Med. Cell. Longevity 2017 (2017) 2467940 http://doi.org/10.1155/2017/2467940.

[15] Q. Cui, J.Q. Wang, Y.G. Assaraf, L. Ren, P. Gupta, L. Wei, C.R. Ashby Jr., D.H. Yang, Z.S. Chen, Modulating ROS to overcome multidrug resistance in cancer, Drug Resist 41 (2018) 1–25 Updates http://doi.org/10.1016/j.drup.2018.11.001 .

[16] J. Kim, J. Kim, J.S. Bae, ROS homeostasis and metabolism: a critical liaison for cancer therapy, Exp. Mol. Med. 48 (2016) e269 http://doi.org/10.1038/emm.2016.119.

[17] D. Trachootham, J. Alexandre, P. Huang, Targeting cancer cells by ROS-mediated mechanisms: a radical therapeutic approach? Nat. Rev. Drug Discov. 8 (2009) 579–591 http://doi.org/10.1038/nrd2803.

[18] M. Fan, Y. Wen, D. Ye, Z. Jin, P. Zhao, D. Chen, X. Lu, Q. He, Acid-responsive H2 -releasing 2D MgB2 nanosheet for therapeutic synergy and side effect attenuation of gastric cancer chemotherapy, Adv. Healthcare Mater. 8 (2019) e1900157 http://doi.org/10.1002/adhm.201900157.

[19] T. Yang, Z. Jin, Z. Wang, P. Zhao, B. Zhao, M. Fan, L. Chen, T. Wang, B.-.L. Su, Q. He, Intratumoral high-payload delivery and acid-responsive release of H2 for efficient cancer therapy using the ammonia borane-loaded mesoporous silica nanomedicine, Appl. Mater 11 (2018) 136–143 Today http://doi.org/10.1016/j.apmt.2018.01.008 .

[20] P. Zhao, Z. Jin, Q. Chen, T. Yang, D. Chen, J. Meng, X. Lu, Z. Gu, Q. He, Local generation of hydrogen for enhanced photothermal therapy, Nat. Commun. 9 (2018) 4241 http://doi.org/10.1038/s41467-018-06630-2.

[21] L. Kong, C. Chen, F. Mou, Y. Feng, M. You, Y. Yin, J. Guan, Magnesium particles coated with mesoporous nanoshells as sustainable therapeutic-hydrogen suppliers to scavenge continuously generated hydroxyl radicals in long term, Part. Part. Sys. Charact. 36 (2019) 1800424 http://doi.org/10.1002/ppsc.201800424.

[22] G. Zhou, Y.S. Wang, Z. Jin, P. Zhao, H. Zhang, Y. Wen, Q. He, Porphyrin–palladium hydride MOF nanoparticles for tumor-targeting photoacoustic imaging-guided hydrogenothermal cancer therapy, Nanoscale Horiz 4 (2019) 1185–1193 http://doi.org/10.1039/c9nh00021f.

[23] Z. Kou, P. Zhao, Z. Wang, Z. Jin, L. Chen, B.-.L. Su, Q. He, Acid-responsive H2-releasing Fe nanoparticles for safe and effective cancer therapy, J. Mater. Chem. B 7 (2019) 2759–2765 http://doi.org/10.1039/c9tb00338j.

[24] L. Kong, N. Rohaizad, M.Z.M. Nasir, J. Guan, M. Pumera, Micromotor-assisted human serum glucose biosensing, Anal. Chem. 91 (2019) 5660–5666 http://doi.org/10.1021/acs.analchem.8b05464.

[25] Y. Wang, C. Zhou, W. Wang, D. Xu, F. Zeng, C. Zhan, J. Gu, M. Li, W. Zhao, J. Zhang, J. Guo, H. Feng, X. Ma, Photocatalytically Powered Matchlike Nanomotor for Light-Guided Active SERS Sensing, Angew. Chem. Int. Ed. 57 (2018) 13110–13113 http://doi.org/10.1002/anie.201807033.

[26] S.K. Srivastava, M. Medina-Sanchez, B. Koch, O.G. Schmidt, Medibots: dual-action biogenic microdaggers for single-cell surgery and drug release, Adv. Mater. 28 (2016) 832–837 http://doi.org/10.1002/adma.201504327.

[27] J. Cui, T.Y. Huang, Z. Luo, P. Testa, H. Gu, X.Z. Chen, B.J. Nelson, L.J. Heyderman, Nanomagnetic encoding of shape-morphing micromachines, Nature 575 (2019) 164–168 http://doi.org/10.1038/s41586-019-1713-2.

[28] X. Yan, Q. Zhou, M. Vincent, Y. Deng, J. Yu, J. Xu, T. Xu, T. Tang, L. Bian, Y.-X.J. Wang, Multifunctional biohybrid magnetite microrobots for imaging-guided therapy, Sci. Robot 2 (2019) eaaq1155 http://doi.org/10.1126/scirobotics.aaq1155 .

[29] J. Shao, M. Xuan, H. Zhang, X. Lin, Z. Wu, Q. He, Chemotaxis-guided hybrid neutrophil micromotors for targeted drug transport, Angew. Chem. Int. Ed. 56 (2017) 12935–12939 http://doi.org/10.1002/anie.201706570.

[30] Z. Wu, Y. Wu, W. He, X. Lin, J. Sun, Q. He, Self-propelled polymer-based multilayer nanorockets for transportation and drug release, Angew. Chem. Int. Ed. 52 (2013) 7000–7003 http://doi.org/10.1002/anie.201301643.

[31] L. Liu, J. Gao, D.A. Wilson, Y. Tu, F. Peng, Fuel-free micro-/nanomotors as intelligent therapeutic agents, Chem. Asian J. 14 (2019) 2325–2335 http://doi.org/10.1002/asia.201900129.

[32] S.M. Beladi-Mousavi, J. Klein, B. Khezri, L. Walder, M. Pumera, Active anion delivery by self-propelled microswimmers, ACS Nano (2020) http://doi.org/10.1021/acsnano.9b09525.

[33] Y. Xing, M. Zhou, X. Du, X. Li, J. Li, T. Xu, X. Zhang, Hollow mesoporous carbon@Pt Janus nanomotors with dual response of H_2O_2 and near-infrared light for active cargo delivery, Appl. Mater. 17 (2019) 85–91 Today http://doi.org/10.1016/j.apmt.2019.07.017 .

[34] S. Wang, K. Liu, F. Wang, F. Peng, Y. Tu, The application of micro- and nanomotors in classified drug delivery, Chem. Asian J. 14 (2019) 2336–2347 http://doi.org/10.1002/asia.201900274.

[35] Y. Tu, F. Peng, X. Sui, Y. Men, P.B. White, J.C.M. van Hest, D.A. Wilson, Self-propelled supramolecular nanomotors with temperature-responsive speed regulation, Nat. Chem. 9 (2016) 480–486 http://doi.org/10.1038/nchem.2674.

[36] B.W. Park, J. Zhuang, O. Yasa, M. Sitti, Multifunctional bacteria-driven microswimmers for targeted active drug delivery, ACS Nano 11 (2017) 8910–8923 http://doi.org/10.1021/acsnano.7b03207.

[37] B.E. de Avila, P. Angsantikul, J. Li, M. Angel Lopez-Ramirez, D.E. Ramirez-Herrera, S. Thamphiwatana, C. Chen, J. Delezuk, R. Samakapiruk, V. Ramez, M. Obonyo, L. Zhang, J. Wang, Micromotor-enabled active drug delivery for in vivo treatment of stomach infection, Nat. Commun. 8 (2017) 272 http://doi.org/10.1038/s41467-017-00309-w.

[38] J. Agudo-Canalejo, T. Adeleke-Larodo, P. Illien, R. Golestanian, Enhanced diffusion and chemotaxis at the nanoscale, Acc. Chem. Res. 51 (2018) 2365–2372 http://doi.org/10.1021/acs.accounts.8b00280.

[39] S. Ghosh, F. Mohajerani, S. Son, D. Velegol, P.J. Butler, A. Sen, Motility of enzyme-powered vesicles, Nano Lett. 19 (2019) 6019–6026 http://doi.org/10.1021/acs.nanolett.9b01830.
[40] F. Peng, Y. Men, Y. Tu, Y. Chen, D.A. Wilson, Nanomotor-based strategy for enhanced penetration across vasculature model, Adv. Funct. Mater. 28 (2018) 1706117 http://doi.org/10.1002/adfm.201706117.
[41] X. Wei, M. Beltrán-Gastélum, E. Karshalev, B. Esteban-Fernández De Ávila, J. Zhou, D. Ran, P. Angsantikul, R.H. Fang, J. Wang, L. Zhang, Biomimetic Micromotor enables active delivery of antigens for oral vaccination, Nano Lett. 19 (2019) 1914–1921 http://doi.org/10.1021/acs.nanolett.8b05051.
[42] Y. Tu, F. Peng, A.A.M. André, Y. Men, M. Srinivas, D.A. Wilson, Biodegradable hybrid stomatocyte nanomotors for drug delivery, ACS Nano 11 (2017) 1957–1963 http://doi.org/10.1021/acsnano.6b08079.
[43] H. Xu, M. Medina-Sanchez, V. Magdanz, L. Schwarz, F. Hebenstreit, O.G. Schmidt, Sperm-hybrid micromotor for targeted drug delivery, ACS Nano 12 (2018) 327–337 http://doi.org/10.1021/acsnano.7b06398.
[44] Y. Wu, X. Lin, Z. Wu, H. Mohwald, Q. He, Self-propelled polymer multilayer Janus capsules for effective drug delivery and light-triggered release, ACS Appl. Mater. Interfaces 6 (2014) 10476–10481 http://doi.org/10.1021/am502458h.
[45] K. Villa, L. Krejčová, F. Novotný, Z. Heger, Z. Sofer, M. Pumera, Cooperative multifunctional self-propelled paramagnetic microrobots with chemical handles for cell manipulation and drug delivery, Adv. Funct. Mater. 28 (2018) 1804343 http://doi.org/10.1002/adfm.201804343.
[46] Y. You, D. Xu, X. Pan, X. Ma, Self-propelled enzymatic nanomotors for enhancing synergetic photodynamic and starvation therapy by self--accelerated cascade reactions, Appl. Mater. 16 (2019) 508–517 Today-http://doi.org/https://doi.org/10.1016/j.apmt.2019.07.008.
[47] F. Peng, Y. Tu, Y. Men, J.C. van Hest, D.A. Wilson, Supramolecular adaptive nanomotors with magnetotaxis behavior, Adv. Mater. 29 (2017) 1604996 http://doi.org/10.1002/adma.201604996.
[48] Z. Wu, J. Li, B.E.-F. de Ávila, T. Li, W. Gao, Q. He, L. Zhang, J. Wang, Water-powered cell-mimicking janus micromotor, Adv. Funct. Mater. 25 (2015) 7497–7501 http://doi.org/10.1002/adfm.201503441.
[49] J. Li, S. Thamphiwatana, W. Liu, B. Esteban-Fernandez de Avila, P. Angsantikul, E. Sandraz, J. Wang, T. Xu, F. Soto, V. Ramez, X. Wang, W. Gao, L. Zhang, J. Wang, Enteric micromotor can selectively position and spontaneously propel in the gastrointestinal tract, ACS Nano 10 (2016) 9536–9542 http://doi.org/10.1021/acsnano.6b04795.
[50] Z. Wu, L. Li, Y. Yang, P. Hu, Y. Li, S.-.Y. Yang, L.V. Wang, W. Gao, A microrobotic system guided by photoacoustic computed tomography for targeted navigation in intestines in vivo, Sci. Robot 4 (2019) eaax0613 http://doi.org/10.1126/scirobotics.aax0613 .
[51] J. Ou, K. Liu, J. Jiang, D.A. Wilson, L. Liu, F. Wang, S. Wang, Y. Tu, F. Peng, Micro-/nanomotors toward biomedical applications: the recent progress in biocompatibility, Small (2020) e1906184 http://doi.org/10.1002/smll.201906184.
[52] C. Chen, E. Karshalev, J. Guan, J. Wang, Magnesium-based micromotors: water-powered propulsion, multifunctionality, and biomedical and environmental applications, Small 14 (2018) e1704252 http://doi.org/10.1002/smll.201704252.
[53] F. Zhang, R. Mundaca-Uribe, H. Gong, B. Esteban-Fernandez de Avila, M. Beltran-Gastelum, E. Karshalev, A. Nourhani, Y. Tong, B. Nguyen, M. Gallot, Y. Zhang, L. Zhang, J. Wang, A macrophage-magnesium hybrid biomotor: fabrication and characterization, Adv. Mater. 31 (2019) e1901828 http://doi.org/10.1002/adma.201901828.
[54] F. Mou, C. Chen, Q. Zhong, Y. Yin, H. Ma, J. Guan, Autonomous motion and temperature-controlled drug delivery of Mg/Pt-Poly(N -isopropylacrylamide) Janus micromotors driven by simulated body fluid and blood plasma, ACS Appl. Mater. Interfaces 6 (2014) 9897–9903 http://doi.org/10.1021/am502729y.
[55] L. Liu, B. Chen, K. Liu, J. Gao, Y. Ye, Z. Wang, N. Qin, D.A. Wilson, Y. Tu, F. Peng, Wireless manipulation of magnetic/piezoelectric micromotors for precise neural stem-like cell stimulation, Adv. Funct. Mater. (2020) 1910108 http://doi.org/10.1002/adfm.201910108.
[56] A.N. Ford Versypt, D.W. Pack, R.D. Braatz, Mathematical modeling of drug delivery from autocatalytically degradable PLGA microspheres–a review, J. Control Release 165 (2013) 29–37 http://doi.org/10.1016/j.jconrel.2012.10.015.
[57] S. Sánchez, L. Soler, J. Katuri, Chemically powered micro- and nanomotors, Angew. Chem. Int. Ed. 54 (2015) 1414–1444 http://doi.org/10.1002/anie.201406096.
[58] H. Wang, G. Zhao, M. Pumera, Blood metabolite strongly suppresses motion of electrochemically deposited catalytic self-propelled microjet engines, Electrochem. Commun. 38 (2014) 128–130 http://doi.org/10.1016/j.elecom.2013.11.013.
[59] G. Zhao, S. Sanchez, O.G. Schmidt, M. Pumera, Poisoning of bubble propelled catalytic micromotors: the chemical environment matters, Nanoscale 5 (2013) 299–2914 http://doi.org/10.1039/c3nr34213a%/Royal Society of Chemistry.
[60] H. Wang, G. Zhao, M. Pumera, Blood electrolytes exhibit a strong influence on the mobility of artificial catalytic microengines, Phys. Chem. Chem. Phys. 15 (2013) 17277 http://doi.org/10.1039/c3cp52726c.
[61] H. Wang, G. Zhao, M. Pumera, Blood proteins strongly reduce the mobility of artificial self-propelled micromotors, Chem. Euro. J. 19 (2013) 16756–16759 http://doi.org/10.1002/chem.201301906.
[62] T. Seo, R. Kurokawa, B. Sato, A convenient method for determining the concentration of hydrogen in water: use of methylene blue with colloidal platinum, Med. Gas Res. 2 (2012) 1 http://doi.org/10.1186/2045-9912-2-1.
[63] G. Yang, O. Jiang, D. Ling, X. Jiang, P. Yuan, G. Zeng, J. Zhu, J. Tian, Y. Weng, D. Wu, MicroRNA-522 reverses drug resistance of doxorubicin-induced HT29 colon cancer cell by targeting ABCB5, Mol. Med. Rep. 12 (2015) 3930–3936 http://doi.org/10.3892/mmr.2015.3890.
[64] L.C. Santos, R. Vogel, J.E. Chipuk, M.R. Birtwistle, G. Stolovitzky, P. Meyer, Mitochondrial origins of fractional control in regulated cell death, Nat. Commun. 10 (2019) 1313 http://doi.org/10.1038/s41467-019-09275-x.
[65] Y. Yang, D. Pan, K. Luo, L. Li, Z. Gu, Biodegradable and amphiphilic block copolymer-doxorubicin conjugate as polymeric nanoscale drug delivery vehicle for breast cancer therapy, Biomaterials 34 (2013) 8430–8443 http://doi.org/10.1016/j.biomaterials.2013.07.037.
[66] H. Sun, J. Su, Q. Meng, Q. Yin, L. Chen, W. Gu, Z. Zhang, H. Yu, P. Zhang, S. Wang, Y. Li, Cancer cell membrane-coated gold nanocages with hyperthermia-triggered drug release and homotypic target inhibit growth and metastasis of breast cancer, Adv. Funct. Mater. 27 (2017) 1604300 -n/a http://doi.org/10.1002/adfm.201604300 .
[67] M. Alibolandi, F. Sadeghi, K. Abnous, F. Atyabi, M. Ramezani, F. Hadizadeh, The chemotherapeutic potential of doxorubicin-loaded PEG-b-PLGA nanopolymersomes in mouse breast cancer model, Eur. J. Pharm. Biopharm. 94 (2015) 521–531 http://doi.org/10.1016/j.ejpb.2015.07.005.
[68] J. Jiang, N. Shen, T. Ci, Z. Tang, Z. Gu, G. Li, X. Chen, Combretastatin A4 nanodrug-induced MMP9 amplification boosts tumor-selective release of doxorubicin prodrug, Adv. Mater. 31 (2019) e1904278 http://doi.org/10.1002/adma.201904278.
[69] M. Li, Z. Tang, D. Zhang, H. Sun, H. Liu, Y. Zhang, Y. Zhang, X. Chen, Doxorubicin-loaded polysaccharide nanoparticles suppress the growth of murine colorectal carcinoma and inhibit the metastasis of murine mammary carcinoma in rodent models, Biomaterials 51 (2015) 161–172 http://doi.org/10.1016/j.biomaterials.2015.02.002.
[70] J. Tian, C. Xiao, B. Huang, C. Wang, W. Zhang, Janus macromolecular brushes for synergistic cascade-amplified photodynamic therapy and enhanced chemotherapy, Acta Biomater. 101 (2020) 495–506 http://doi.org/10.1016/j.actbio.2019.11.018.
[71] H. Gong, L. Cheng, J. Xiang, H. Xu, L. Feng, X. Shi, Z. Liu, Near-infrared absorbing polymeric nanoparticles as a versatile drug carrier for cancer combination therapy, Adv. Funct. Mater. 23 (2013) 6059–6067 http://doi.org/10.1002/adfm.201301555.
[72] F. Wang, Q. Sun, B. Feng, Z. Xu, J. Zhang, J. Xu, L. Lu, H. Yu, M. Wang, Y. Li, W. Zhang, Polydopamine-functionalized graphene oxide loaded with gold nanostars and doxorubicin for combined photothermal and chemotherapy of metastatic breast cancer, Adv. Healthcare Mater. 5 (2016) 2227–2236 http://doi.org/10.1002/adhm.201600283.
[73] H. Deng, K. Song, X. Zhao, Y. Li, F. Wang, J. Zhang, A. Dong, Z. Qin, Tumor microenvironment activated membrane fusogenic liposome with speedy antibody and doxorubicin delivery for synergistic treatment of metastatic tumors, ACS Appl. Mater. Interfaces 9 (2017) 9315–9326 http://doi.org/10.1021/acsami.6b14683.
[74] X. Liu, C. Wang, H. Ma, F. Yu, F. Hu, H. Yuan, Water-responsive hybrid nanoparticles codelivering ICG and DOX effectively treat breast cancer via hyperthermia-aided dox functionality and drug penetration, Adv. Healthcare Mater. 8 (2019) e1801486 http://doi.org/10.1002/adhm.201801486.